EES Batteries

PAPER

View Article Online
View Journal

Cite this: DOI: 10.1039/d6eb00057f

Weakly dissociated lithium salt decouples solvent–anion interfacial dynamics for wide-temperature lithium-ion batteries

Shaoyun Zhou,†[a,b] Zetai Xu,†[a] Chaonan Wang,†[a] Chao Tang,[a,b] Junhua Jian,[b] Meirong Wang,[b] Hong-Bin Yao,[a] Hongchang Jin,*[a] Yuhao Lu*[b] and Hengxing Ji*[a]

Developing lithium-ion batteries (LIBs) operable across extreme temperatures (−40 to 60 °C) is imperative for electric vehicles and space technologies, yet hindered by incompatible interphasial requirements: cathode–electrolyte interphase (CEI) degradation at high temperatures and anode solid-electrolyte interphase (SEI) impedance surge under subzero conditions. Here, we report a novel dual-salt electrolyte composed of weakly dissociated $LiPO_2F_2$ (LiDFP) and commonly used $LiPF_6$ in an ethyl acetate (EA)/ethylene carbonate (EC) co-solvent, enabling wide-temperature LIB operation with exceptional interphasial stability. LiDFP with elevated solubility renders contact ion pairs and aggregates surrounding Li^+, enriching $PO_2F_2^-$ coordination within the Li^+ solvation shell. This unique solvation structure promotes the preferential decomposition of $PO_2F_2^-$ anions at electrode surfaces, forming thin, dense CEI/SEI layers dominated by Li_3PO_4 and LiF, which simultaneously enhance interphasial robustness and Li^+ transport. As a result, 5 Ah NCM613||graphite pouch cells deliver over 80% capacity retention after 200 cycles at 60 °C and maintain 57% reversible capacity at −40 °C, while the cell using the $LiPF_6$-EC electrolyte retains 80% capacity after only 200 cycles at 45 °C. By decoupling anion-mediated interfacial regulation from solvent-centric limitations, this work establishes a universal electrolyte paradigm to achieve intrinsically stable, wide-temperature LIBs.

Received 10th March 2026,
Accepted 5th May 2026

DOI: 10.1039/d6eb00057f

rsc.li/EESBatteries

Broader context

Developing lithium-ion batteries for extreme temperatures (−40 to 60 °C) is critical for electric vehicles and space exploration. A key challenge lies in stabilizing the interfaces at both electrodes simultaneously under such conditions. We report a dual-salt electrolyte using $LiPO_2F_2$ and $LiPF_6$ in ethyl acetate/ethylene carbonate solvents. This design enriches $PO_2F_2^-$ anions around Li^+ ions, prompting their preferential decomposition to form robust, ion-conductive interphases rich in Li_3PO_4 and LiF. Consequently, 5 Ah graphite||NCM613 cells retain >80% capacity after 200 cycles at 60 °C and deliver 57% room-temperature capacity at −40 °C, outperforming conventional electrolytes. This work provides a universal strategy for designing wide-temperature batteries through anion-mediated interfacial regulation.

Introduction

The development of lithium-ion batteries (LIBs) capable of stable operation across a wide temperature window remains a formidable challenge, primarily due to interphasial instabilities at both the cathode and anode.[1–5] At high temperatures (>45 °C), both the cathode–electrolyte interphase (CEI) and the anode solid-electrolyte interphase (SEI) become unstable. They undergo repeated dissolution/reformation, consuming cyclable Li^+. The CEI degradation accelerates transition metal (TM) dissolution from cathodes (*e.g.*, NCM ternary material), which in turn facilitates the breakdown and subsequent rebuilding of the CEI and SEI.[6,7] Such continuous rebuilds of the CEI and SEI concurrently generate thick and resistive coatings at the cathode and anode surfaces, increasing impedance and reducing achievable battery capacity, particularly at low temperatures. It is noteworthy that the raised impedance at the anode side by an SEI tends to result in lithium plating when charging the battery at low temperatures. Lithium plating is a primary cause of battery failure and safety hazards.[8–11] Thermally stable and Li^+ conductive CEI and SEI layers are essential to

[a]*Hefei National Research Center for Physical Sciences at the Microscale, School of Chemistry and Materials Science, iChEM, University of Science and Technology of China; Hefei, Anhui 230026, China*
[b]*Ningde Amperex Technology Limited (ATL), Key laboratory of consumer lithium-ion battery in Fujian, Ningde, 352100, China*
†These authors contributed equally to this work.

LIB functioning in a wide temperature range, which is of central importance in battery research.[12–14] As both the CEI and SEI are the products of electrolyte decomposition, designing functional electrolytes that can generate a thermally stable CEI under highly oxidative potential in the cathode and a Li^+ conductive SEI under highly reductive potential in the anode becomes essential.

However, current electrolyte formulations struggle to balance these requirements, as thermally and electrochemically stable electrode–electrolyte interphases typically sacrifice interphasial Li^+ mobility. Furthermore, because the electrolyte is in contact with both the cathode and anode, almost no electrolyte design can form a stable CEI without compromising the SEI kinetics.[15–17] From an electrolyte perspective, the inherent limitations of widely used $LiPF_6$ in ethylene carbonate (EC)-based electrolytes further complicate interfacial control.[18,19] The strong dissociation of $LiPF_6$ in EC-dominated solvation structures results in solvent-rich coordination shells, favoring organic-rich CEI/SEI layers with excessive thickness and low Li^+ conductivity.[20–22] While cosolvents or additives (*e.g.*, 1,1,2,2-tetrafluoroethyl-2,2,3,3-tetrafluoropropyl ether, fluoroethylene carbonate) can partially regulate solvation structures by enhancing anion participation, such approaches often prioritize either CEI's thermal stability or SEI's Li^+ conductivity. For instance, anion-coordinating additives like lithium bis(oxalate)borate (LiBOB) yield an integrative and thermally stable CEI but increase SEI resistivity, whereas some agents (*e.g.*, vinylene carbonate) generate a mechanically robust SEI with a fragile CEI at high temperature. This trade-off underscores the need for lithium salts with high solubility but low dissociation degrees to decouple the solvation dynamics from interfacial reactions.[23–27]

Lithium difluorophosphate (LiDFP), a weakly dissociated salt, presents a promising alternative. Its limited dissociation reduces solvent-dominated coordination, promoting anion-derived interphasial components (*e.g.*, LiF, Li_3PO_4) that can enhance both CEI thermal stability and SEI ionic transport. However, LiDFP's low solubility in carbonate solvents (~0.1 M) limits its practical utility. Previous studies demonstrate that a trace amount of LiDFP additive improves interphasial properties, yet the low concentration fails to fully exploit its potential. Enhancing LiDFP solubility without compromising ionic conductivity or low-temperature fluidity could unlock its dual-functionality. This goal requires solvents that can both dissolve LiDFP at high concentrations and preserve broad liquidus ranges, a condition not satisfied by conventional carbonate solvents.

In this study, we report a weakly solvating electrolyte for wide-temperature LIBs by employing a dual-salt electrolyte, which contains weakly dissociated LiDFP in synergy with $LiPF_6$, coupled with a high-dielectric-constant ethyl acetate (EA)/EC co-solvent. EA incorporation enhances LiDFP solubility in the carbonate-based solvents to 1.4 M while significantly decreasing electrolyte melting points. In the 0.5 M LiDFP/0.5 M $LiPF_6$ (EA/EC) electrolyte, LiDFP predominantly exists as contact ion pairs (CIPs) and aggregates (AGGs) substantially increasing $PO_2F_2^-$ anion coordination numbers in the primary solvation shells surrounding the Li^+. This solvation structure allows $PO_2F_2^-$ anions to preferentially decompose at electrode surfaces to form thin, dense, inorganic-rich (Li_3PO_4 and LiF) CEI/SEI layers that effectively enhance interphasial stability and kinetics. In 5 Ah pouch cells (NCM613‖graphite), this electrolyte demonstrates exceptional thermal stability and low-temperature performance: >80% capacity retention after 200 cycles at 60 °C and 57% reversible capacity retention at −40 °C, respectively. By strategically regulating lithium salt dissociation and solvation structures, this work provides an industrially viable electrolyte design strategy for developing wide-temperature LIBs.

Results and discussion

EA co-solvent enhances LiDFP solubility for improved electrode interfaces

LiDFP exhibits low solubility in common solvents such as EC, diethyl carbonate (DEC), and dimethyl carbonate (DMC), limiting its effectiveness in optimizing electrode interface structures. As lithium salt solubility typically correlates with solvent dielectric constant and donor number (DN),[28,29] solvents with high dielectric constants and DN values were screened to enhance LiDFP solubility in carbonate-based electrolytes (Table S1). These included dimethyl sulfoxide (DMSO), triethyl phosphate (TEP), dimethoxyethane (DME), sulfolane (SL), and EA. LiDFP demonstrated high solubility (>9 wt%) in all screened solvents.[30–33] However, DMSO, TEP, and SL exhibited excessive viscosity, while DME showed limited oxidative stability at the cathode. These solvents also present pronounced solvent co-intercalation risks with graphite anodes.[34–38] Consequently, EA emerges as a promising alternative to conventional carbonates due to its broad liquidus range (−83.6 to 77.1 °C), low viscosity, and favorable electrochemical stability.[39] Plus, the solubility of LiDFP in the EA co-solvent is increased to 1.4 M, around twenty times higher than that in EC (<0.06 M, Fig. 1c).

The surface electrostatic potential of EA relative to conventional solvents and electrochemical windows of LiDFP relative to $LiPF_6$ were investigated. Density functional theory (DFT) calculations indicate that EA exhibits reduced cathodic electrostatic potential *versus* EC, reflecting weaker polarity and diminished Li^+ solvation capability (Fig. 1a).[40] Frontier molecular orbital analysis reveals that LiDFP possesses a higher HOMO energy (−8.71 eV) than $LiPF_6$, signifying its preferential oxidative decomposition for CEI formation (Fig. 1b). Linear sweep voltammetry (LSV) confirmed interfacial decomposition of LiDFP: 0.5 M LiDFP-EA/EC (7 : 3) electrolyte showed a distinct oxidation peak at ~3.5 V corresponding to CEI formation (Fig. 1d).[41] Cathodic LSV profiles revealed suppressed EA reduction currents at ~2.5 V with increasing LiDFP content, indicating its critical role in anode passivation (Fig. 1e).

Low LiDFP dissociation enables anion-rich interfaces

Li^+ coordination in electrolytes was probed *via* Raman spectroscopy (Fig. S1). In contrast to $LiPF_6$/EA that exhibited

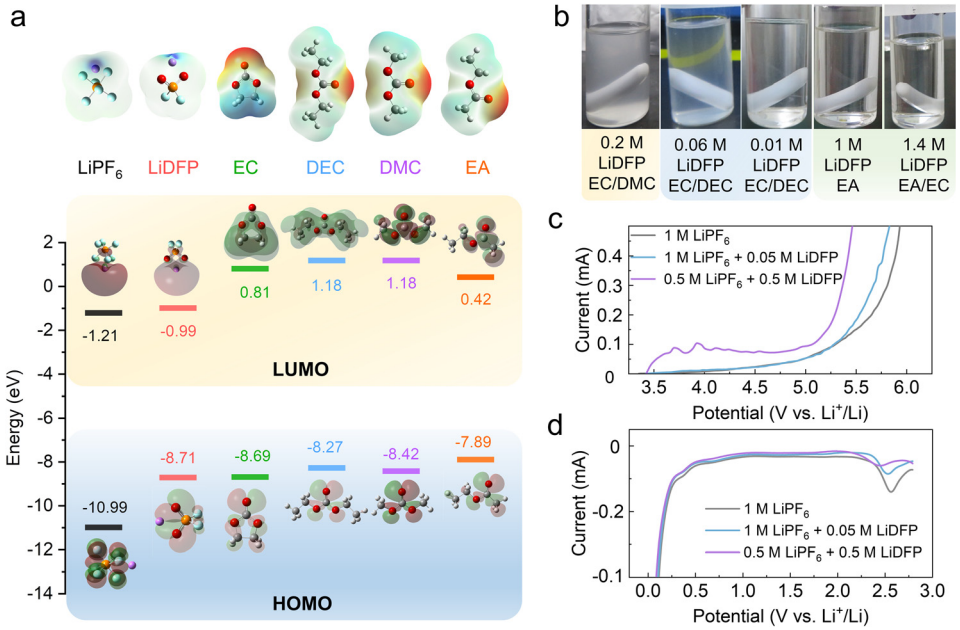

Fig. 1 (a) Calculated electrostatic potentials for EC, DEC, DMC and EA; (b) frontier molecular orbital (HOMO/LUMO) energy levels for $LiPF_6$ and LiDFP; (c) visual comparison of electrolytes with varying LiDFP concentrations in EC-based (EC/DMC, EC/DEC) and EA-based (EA, EA/EC) solvent systems; (d) anodic LSV profiles (3.0–6.0 V *vs.* Li^+/Li, 1 mV s^{-1}) and (e) cathodic LSV profiles (3.0–0.01 V *vs.* Li^+/Li, 1 mV s^{-1}) of 1 M $LiPF_6$, 1 M $LiPF_6$ + 0.05 M LiDFP, and 0.5 M $LiPF_6$ + 0.5 M LiDFP in the EA/EC (7 : 3 v/v) electrolyte.

characteristic PF_6^- vibration (741 cm^{-1}), the Raman spectrum of LiDFP/EA presented concentration-dependent P–O bond signals. Critically, LiDFP caused negligible EA solvent peak shifts (848 cm^{-1} and 2940 cm^{-1}), contrasting with $LiPF_6$-induced peak broadening and wavenumber increases, indicating weaker Li^+–$PO_2F_2^-$ coordination *versus* Li^+–PF_6^- inter-

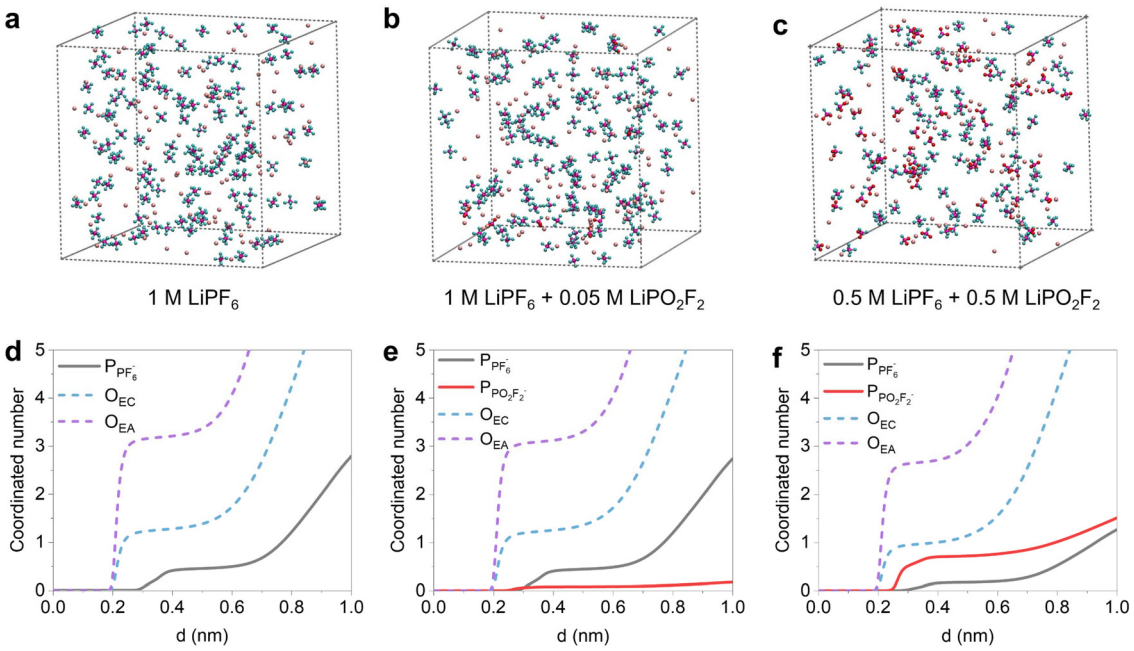

Fig. 2 (a–c) Representative MD simulation snapshots depicting solvation structures in (a) 1 M $LiPF_6$ EA/EC, (b) 1 M $LiPF_6$ + 0.05 M LiDFP EA/EC, and (c) 0.5 M $LiPF_6$ + 0.5 M LiDFP EA/EC. (d–f) Calculated Li^+ coordination numbers for (d) 1 M $LiPF_6$ EA/EC, (e) 1 M $LiPF_6$ + 0.05 M LiDFP EA/EC, and (f) 0.5 M $LiPF_6$ + 0.5 M LiDFP EA/EC.

actions. Besides, we included the binding energies with Li^+ for EC (−2.37 eV), ethyl methyl carbonate (EMC, −2.39 eV), DEC (−2.34 eV), DMC (−2.41 eV), EA (−2.20 eV), PF_6^- (−4.98 eV), and $PO_2F_2^-$ (−5.68 eV) (as shown in Fig. S2). The binding energy between Li^+ and $PO_2F_2^-$ anions is higher than that with PF_6^-, and significantly higher than those with common solvents including EC and EA. Therefore, LiDFP acts as a weakly dissociating salt and disrupts the dominance of solvent coordination, resulting in a solvation structure in the electrolyte that is rich in CIPs and AGGs.[42] However, low dissociation typically compromises ionic conductivity. We measured the ionic conductivities and revealed fundamental differences between $LiPF_6$ and LiDFP in EA and EA/EC (7 : 3 v/v) systems (Table S2). Despite the high LiDFP solubilities in EA (1.1 M) and EA/EC (1.5 M), the electrolyte conductivities remained low (0.04 and 0.62 mS cm^{-1}, respectively). LiDFP addition substantially reduced conductivity even in the $LiPF_6$–LiDFP dual-salt electrolyte, indicating limited dissociation of the salts. We thus investigated three types of salts, 1 M $LiPF_6$, 1 M $LiPF_6$ + 0.05 M LiDFP, and 0.5 M $LiPF_6$ + 0.5 M LiDFP, dissolved in EA/EC (7 : 3 v/v) to achieve a favorable electrolyte conductivity.

Molecular dynamics simulations elucidated Li^+ solvation structures. In dual-salt systems, increasing LiDFP content reduced Li^+ coordination with PF_6^-, EC, and EA while enhancing $PO_2F_2^-$ coordination. $PO_2F_2^-/PF_6^-$ and $PO_2F_2^-$/solvent ratios increased significantly with LiDFP/$LiPF_6$ ratio (Fig. 2 and Table S3). For single-salt systems, 1 M $LiPF_6$-EA showed Li^+ coordination with 3.8 EA molecules and 0.8 PF_6^- anions, indicating predominant solvent-separated ion pairs (SSIPs) (Fig. S3). Conversely, 1 M LiDFP-EA showed Li^+ coordination with 2.5 EA molecules and 1.6 $PO_2F_2^-$ anions, with anion coordination >1 signifying increased CIPs and AGGs. This anion-enriched structure promotes $PO_2F_2^-$ participation in interfacial reactions, suppressing solvent decomposition. Collectively, these results demonstrate that the preferential formation of phosphate-rich interphases inhibits parasitic reactions—highlighting LiDFP's functionality *via* low dissociation and anion-dominated solvation. To experimentally validate the anion coordination predicted by molecular dynamics (MD) simulations, we performed Raman spectroscopy and deconvolution analysis on electrolytes with varying LiDFP content as shown in Fig. S4 and S5 (EA/EC co-solvent, 1 M $LiPF_6$ in EA/EC electrolyte,

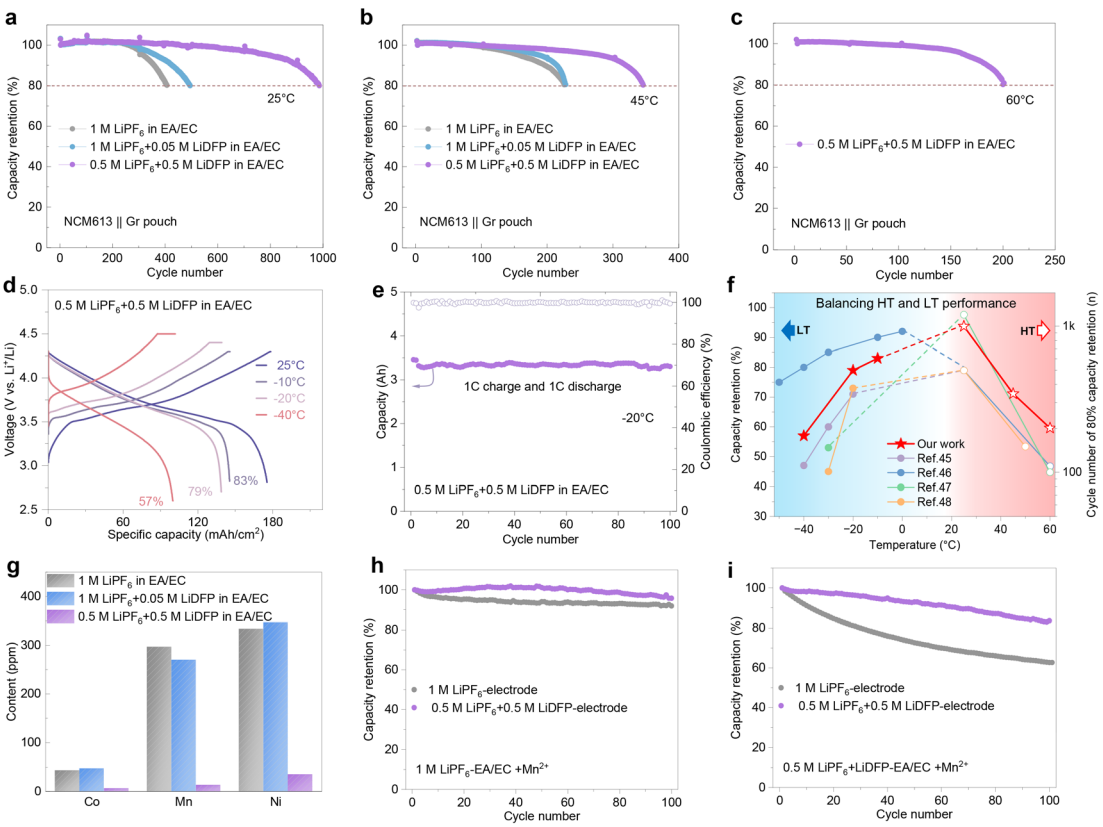

Fig. 3 (a–c) Cycling performance of pouch cells at 25 °C, 45 °C, and 60 °C, respectively. (d) Voltage profiles of pouch cells with 0.5 M $LiPF_6$ + 0.5 M LiDFP EA/EC at −40 to 25 °C. (e) Low-temperature cycling performance in 0.5 M $LiPF_6$ + 0.5 M LiDFP EA/EC electrolyte (−20 °C, 1C rate). (f) Benchmarking of the reported Gr-based full cells: cycle durability at high temperature and capacity retention at low temperature. (g) TM deposition concentrations on anodes after 280 cycles (25 °C) quantified by ICP. (h and i) Cycling performance of cells reassembled with Mn^{2+}-added electrolytes: (h) LiPF6 baseline and (i) $LiPF_6$/LiDFP dual-salt system.

1 M $LiPF_6$ + 0.05 M LiDFP in EA/EC electrolyte, and 0.5 M $LiPF_6$ + 0.5 M LiDFP in EA/EC electrolyte). The distribution confirms that LiDFP exists predominantly as CIPs and AGGs, markedly increasing the $PO_2F_2^-$ coordination number in the primary Li^+ solvation shell, in excellent agreement with the MD simulations.[43,44]

LiDFP enables superior wide-temperature cycling and stability

Battery tests evaluated LiDFP's impact on wide-temperature performance. In 5 Ah NCM||Gr pouch cells mixed-salt electrolyte was used (Fig. S6). High-temperature storage (60 °C) showed that cells with single-salt $LiPF_6$ electrolyte exhibited 9.7% expansion after 6 days and 17.2% after 24 days (Fig. S7). LiDFP addition mitigated expansion: adding 0.05 M LiDFP showed 10.4% expansion after 24 days, while adding 0.5 M LiDFP showed only 3.8%, confirming enhanced high-temperature stability. At 25 °C (Fig. 3a), the 1 M $LiPF_6$ cell maintained 80% capacity after 407 cycles. The 1 M $LiPF_6$ + 0.05 M LiDFP electrolyte extended this to 495 cycles. The 0.5 M $LiPF_6$ + 0.5 M LiDFP electrolyte exhibited superior stability, maintaining 80% capacity after 986 cycles (0.02% average decay/cycle). High-temperature cycling (45 °C, Fig. 3b) showed cells achieving 80% retention after 226, 228, and 346 cycles, respectively. At 60 °C, the 0.5 M $LiPF_6$ + 0.5 M LiDFP cell maintained 80% capacity after 200 cycles (Fig. 3c). Thus, LiDFP significantly enhances both room- and high-temperature cycling. Rate performance (Fig. S8) confirmed optimal performance for 0.5 M $LiPF_6$ + 0.5 M LiDFP at 0.3C to 4C, retaining 92.7% capacity at 4C. Low-temperature testing demonstrated 79% and 57% capacity retention at −20 °C and −40 °C, respectively, with negligible decay after 100 cycles at −20 °C (Fig. 3d and e). These results indicate that the $LiPF_6$/LiDFP dual-salt electrolyte

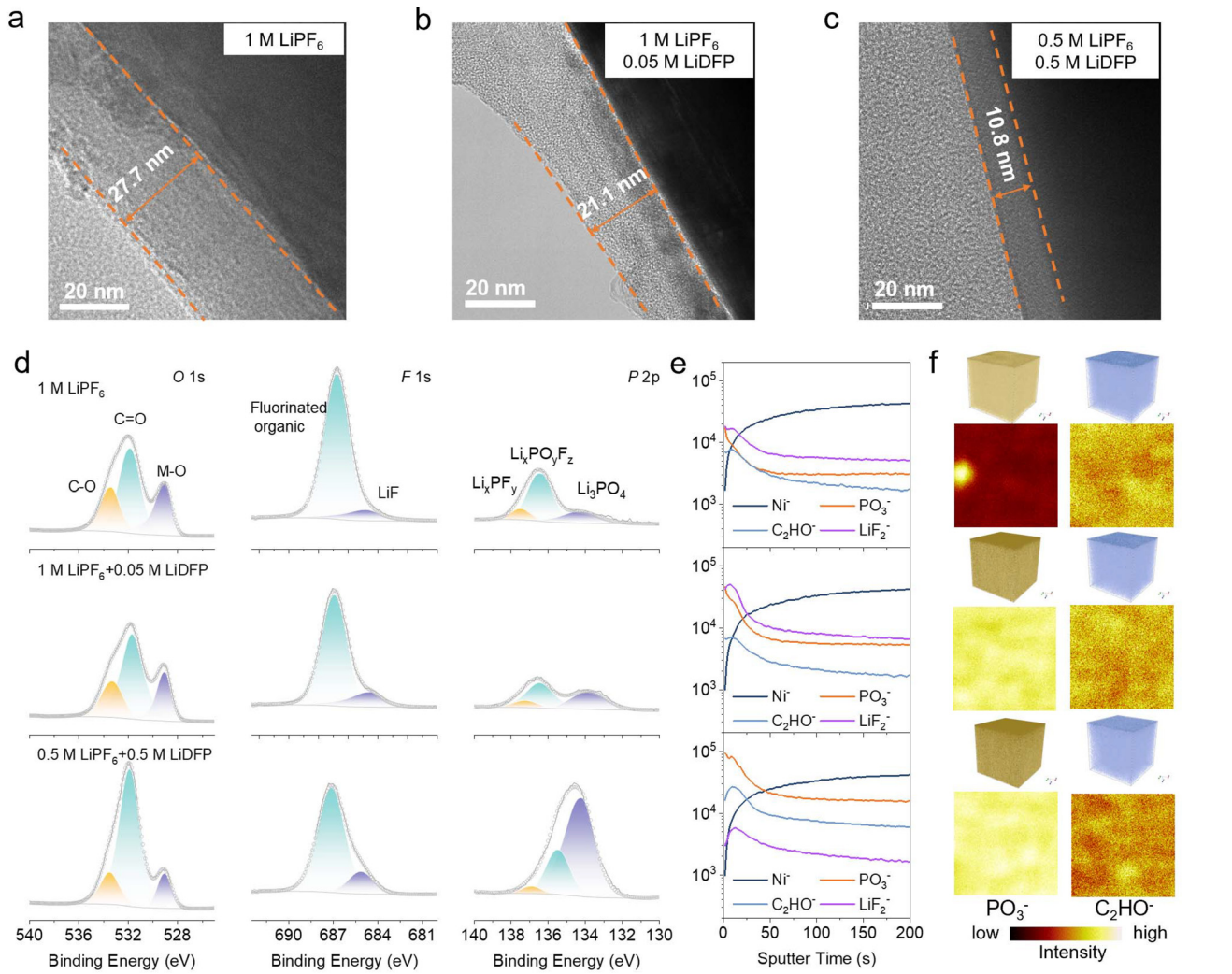

Fig. 4 Representative TEM images of cathodes after initial formation in (a) 1 M $LiPF_6$ EA/EC, (b) 1 M $LiPF_6$ + 0.05 M LiDFP EA/EC, and (c) 0.5 M $LiPF_6$ + 0.5 M LiDFP EA/EC electrolytes; (d) comparative XPS spectra of cathodes cycled in different electrolytes. (e) Depth distribution curves of various secondary ion species of the cathodes with different electrolytes after the initial formation obtained by ToF-SIMS; (f) 3D reconstruction and 2D mapping of interphasial PO_3^- and C_2HO^- secondary ion distributions for NCM613 cathodes.

achieves superior high/low-temperature performance balance *versus* the literature (Fig. 3f and Table S4).[45–48]

The dissolution of cathode TM ions induces detrimental crosstalk effects, compromising battery cycle life. To evaluate the suppression of TM dissolution by the LiDFP-derived interphase, we quantified TM deposition on the graphite anode surface *via* inductively coupled plasma (ICP) analysis. Cells exhibiting negligible capacity fade when cycled 280 times at 25 °C were disassembled prior to significant interphase degradation. Fig. 3g depicts the TM content (Ni, Mn, Co) on the graphite anode. Compared to pouch cells employing $LiPF_6$-only electrolyte or electrolyte with 0.05 M LiDFP additive, cells utilizing the $LiPF_6$/LiDFP dual-salt electrolyte exhibited significantly reduced TM deposition on graphite. This inhibition prevents persistent solvent decomposition at the anode, thereby suppressing SEI growth and interphasial impedance increase.[49,50] Furthermore, we simulated cathode-derived TM dissolution by introducing Mn^{2+} into the electrolyte, assessing their impact on the SEI formed in $LiPF_6$ and $LiPF_6$/LiDFP dual-salt systems. Full-cell cycling performance tests were conducted on reassembled cells employing electrolytes containing 20 mM Mn^{2+} in either 1 M $LiPF_6$ EA/EC or 0.5 M $LiPF_6$ + 0.5 M LiDFP EA/EC, as illustrated in Fig. 3h and i. The results demonstrate that the interphase derived from the $LiPF_6$/LiDFP dual-salt electrolyte possesses superior resistance to TM ion interference, underscoring its role in stabilizing the CEI/SEI.

LiDFP forms a thin, inorganic-rich CEI

Given LiDFP's interphasial optimization at both electrodes, we characterized interphase structures. Transmission electron microscopy (TEM) images (Fig. 4a–c) and elemental maps (Fig. S9–11) reveal that the CEI formed in $LiPF_6$ electrolyte is

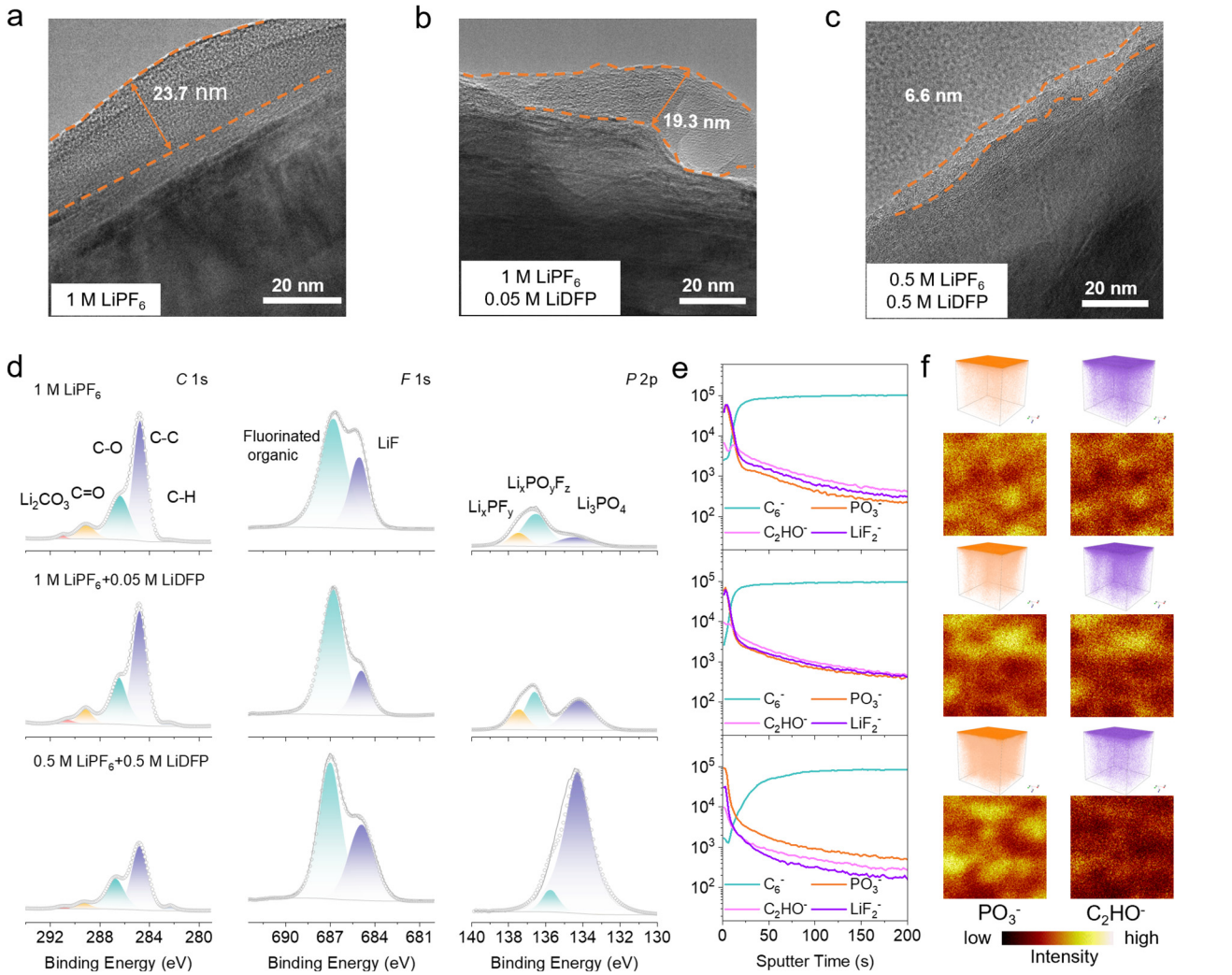

Fig. 5 Representative TEM images of anodes after initial formation in (a) 1 M $LiPF_6$ EA/EC, (b) 1 M $LiPF_6$ + 0.05 M LiDFP EA/EC, and (c) 0.5 M $LiPF_6$ + 0.5 M LiDFP EA/EC electrolytes; (d) comparative XPS spectra of cathodes cycled in different electrolytes. (e) Depth distribution curves of various secondary ion species of the anodes with different electrolytes after the initial formation obtained by ToF-SIMS; (f) 3D reconstruction and 2D mapping of interphasial PO_3^- and C_2HO^- secondary ion distributions for graphite cathodes.

thick (27.7 nm) and inhomogeneous, indicative of unstable interfacial reactions. Incorporating 0.05 M LiDFP moderately reduced the CEI thickness (21.1 nm) and improved compactness. Conversely, the $LiPF_6$/LiDFP dual-salt electrolyte formed a thinner (10.8 nm), uniform CEI on cathodes. X-ray photoelectron spectroscopy (XPS) and time of flight secondary ion mass spectrometry (ToF-SIMS) analyses (Fig. 4d) confirm that all three electrolyte systems yield CEIs containing substantial C–O and C═O species on NCM cathodes.[10] The O 1s peak at 529.2 eV corresponds to lithium/TM oxides (M–O), reflecting electrolyte–TM reactions.[51] The dual-salt electrolyte reduced M–O content in the CEI, indicating diminished cathode material exposure. LiDFP introduction enhanced CEI compactness, suppressing electrolyte oxidation by delithiated cathodes and TM dissolution. F 1s and P 2p spectra show that the dual-salt electrolyte significantly increased Li_3PO_4 and LiF content in the CEI. These inorganic components bolster CEI stability, while LiF's high Li^+ mobility and Li_3PO_4's superior ionic conductivity collectively improve interphasial ion transport and reduce organic fluorinated content.[52,53] ToF-SIMS depth profiling (Fig. 4e) reveals the CEI composition: inorganic species (LiF_2^-, PO_3^-) and organic fragments (C_2HO^-) constitute the interphase.[54] Elevated LiDFP content amplified PO_3^- signals while attenuating C_2HO^- signals, demonstrating LiDFP's efficacy in suppressing solvent decomposition. 3D visualization and 2D distribution of PO_3^- and C_2HO^- ions (Fig. 4f) confirm that the dual-salt electrolyte yields an optimized cathode interphase structure post formation.

LiDFP promotes a thin, inorganic-rich SEI

Beyond the CEI, the anode SEI critically governs electrochemical performance. We systematically characterized the SEI morphology and composition from different electrolytes. TEM results (Fig. 5a–c) show that the $LiPF_6$-derived SEI is thicker (23.7 nm), and the addition of 0.05 M LiDFP reduces the SEI thickness but makes it uneven. The dual-salt electrolyte formed a thinner (6.6 nm), homogeneous SEI. XPS and ToF-SIMS analyses elucidated the SEI composition (Fig. 5d): C 1s spectra feature predominant organic components (C–C, C–O, C═O) in all systems, yet the dual-salt electrolyte substantially attenuated these signals. F 1s and P 2p spectra confirm that LiDFP promotes inorganic Li_3PO_4 and LiF formation at the anode interphase, with Li_3PO_4 being the primary SEI product from LiDFP decomposition. Depth profiles and 3D/2D distributions of PO_3^- and C_2HO^- ions (Fig. 5e and f) illustrate component stratification from the surface to bulk. The graphite interphase comprises inorganic (LiF_2^-, PO_3^-) and organic (C_2HO^-) species. The dual-salt electrolyte yields an inorganic-rich (LiF_2^-, PO_3^-) SEI with reduced organic content, favoring robust interphasial kinetics. Hence, LiDFP as a mixed main salt significantly enhances battery performance by forming a dense and stable CEI and a SEI rich in Li_3PO_4 and LiF inorganic components at both electrode interphases. These interphasial analyses indicate that the high concentration and weak dissociation of LiDFP in the electrolyte facilitate the formation of a phosphate-rich and organic-lean CEI/SEI, which significantly enhances interphase stability and prolongs battery life.

Conclusions

We employed a dual-salt electrolyte (0.5 M LiDFP/0.5 M $LiPF_6$) in an EA/EC co-solvent, which rendered stable wide-temperature lithium-ion battery operation. The weak dissociation of LiDFP predominantly forms CIPs and AGGs, substantially increasing the $PO_2F_2^-$ anion coordination number within the primary solvation shell surrounding Li^+. This regulated solvation structure drives preferential anion decomposition at electrode surfaces, generating thin, dense, inorganic-rich (Li_3PO_4 and LiF) CEI and SEI layers. Consequently, 5 Ah NCM613‖graphite pouch cells exhibit >80% capacity retention after 200 cycles at 60 °C and deliver 57% reversible capacity at −40 °C. This work demonstrates an industrially viable electrolyte design strategy for wide-temperature batteries through precise control of lithium salt dissociation and solvation dynamics.

Experimental

Electrolyte and electrode preparation

The raw materials for the electrolytes were purchased from Guangzhou Tinci Materials Technology Co., Ltd in battery-grade specification. The EA/EC (7 : 3 v/v) solvent system was employed with varying $LiPF_6$/LiDFP ratios (1 M $LiPF_6$, 1 M $LiPF_6$ + 0.05 M LiDFP, and 0.5 M $LiPF_6$ + 0.5 M LiDFP).

The NCM613 cathode contained 96.5 wt% NCM613 material, super P as the conductive agent and PVDF as the binder. The graphite anode contained 97 wt% artificial graphite and SBR as the binder. The size of these pouch cells is 8.3 mm × 66 mm × 79 mm, the designed capacity is about 4.8 Ah, and the charging/discharging voltage range is 3.0–4.28 V. The NCM613‖graphite pouch cells were assembled in the pouch-cell production line and each pouch cell was filled with 20 g of the electrolyte. The entire electrode and pouch cell preparation procedure was scrupulously conducted in a dry room environment, assured by maintaining a dew point below −40 °C to prevent any moisture-induced compromises during the production process. The half cells were meticulously assembled into 2032-type coin cells, incorporating a polypropylene (PP) separator saturated with 50 μL of electrolyte. The intricate assembly process took place within the inert environment of an argon-filled glovebox, where both water and oxygen levels were stringently controlled to remain below 0.1 ppm.

Electrochemical measurements

Linear sweep voltammetry (LSV) was carried out to evaluate the redox potential of the electrolytes. The positive scan was conducted from the open circuit potential to 6 V (*vs.* Li^+/Li) with Pt as the working electrode and Li metal as the counter electrode and reference electrode, and the negative scan was

conducted from the open circuit potential to 0.01 V. The scanning rate was 1 mV s^{-1}. The cycle performance tests at 25 °C, 45 °C and 60 °C were performed with a Neware battery test system. The cycling protocol was set up as follows: First, the cell was charged to 4.28 V at 1C, and then charged at a constant voltage of 4.28 V until the current reached 0.05C followed by 5 min of rest. Second, it was discharged to 3.0 V at 1C followed by 5 min of rest. The above steps were repeated until the discharge capacity retention reached 80%. It should be noted that a cycle for 0.2C charging–discharging was conducted every 100 cycles.

Material characterization

Raman spectra were acquired on a HORIBA HR Evolution featuring a 532 nm laser source for excitation. TEM images were obtained using a high-resolution transmission electron microscope (Talos F200X). ICP-AES tests were conducted on a PE ICP 7000DV. XPS measurements were performed using depth-profiling X-ray photoelectron spectroscopy (ESCALAB 250Xi). Specially designed airtight apparatus was used to transfer the electrodes into the XPS system without exposure to air. TOF-SIMS was performed on a ToF-SIMS5-100 instrument in the vacuum interconnected nanotech workstation SINANO, CAS. For the SEI study, the electrodes after cycling were disassembled in a glove box and rinsed several times with DMC to remove residual electrolytes.

Calculation methods

Molecular dynamics (MD) simulations for all electrolyte systems were performed with the GROMACS simulation package, version 2019.3 using optimized potentials for liquid simulations-all atom (OPLS-AA) force fields, while the bonded and non-bonded parameters for solvent molecules were obtained from LigParGen, a publicly accessible web server.[55,56] The partial atomic charges for solvents were calculated using the Gaussian 16 program at the PBE0/def2TZVP level and following Hirshfeld population analysis. CM5 charges were mapped with Multiwfn code and scaled by a factor of 1.2.[57,58] For each simulation system, a total of 1500 molecules including solvent and salt components were initially packed randomly in a cubic box with a primary size of 65 Å × 65 Å × 65 Å using PACKMOL.[59] For facilitating the equilibration of the system, an annealing process was conducted with an NPT ensemble before production simulation, in which the system was heated to 400 K and kept for 1 ns, then cooled down to 298 K within a time interval of 1 ns and kept at 298 K for another 1 ns. After that, production simulation running for 5 ns was also performed in the NPT ensemble, under a Nose–Hoover thermostat and a Parrinello–Rahman barostat to maintain a pressure of 1 atm and a temperature of 298 K. Further results were analyzed from the trajectory data using the GROMACS tool-suites and visual molecular dynamics (VMD) software.[60] The relevant quantum chemical (QC) calculations shown in Fig. S2 were conducted with Gaussian 16 (Revision C.01) using density functional theory (DFT) at the PBE0/ma-TZVP level.

Conflicts of interest

There are no conflicts to declare.

Data availability

The data supporting the findings of this study are available from the corresponding author upon reasonable request. Supplementary information (SI) is available. See DOI: https://doi.org/10.1039/d6eb00057f.

Acknowledgements

We appreciate the funding support from the National Natural Science Foundation of China (22125902, 22109150, and 22279126), the Anhui Science Fund for Distinguished Young Scholars (2408085J009), USTC Tang Scholar, the Fundamental Research Funds for the Central Universities (WK2490000002), and the Major Industrial Innovation Program of Anhui Province (BJ9980008003). We thank Nano-X (SINANO, CAS) for assistance with characterization. The simulations were performed on the robotic AI-Scientist platform of the Chinese Academy of Sciences.

References

1 M. Li, J. Lu, Z. Chen and K. Amine, *Adv. Mater.*, 2018, **30**, 1800561.
2 M. Winter, B. Barnett and K. Xu, *Chem. Rev.*, 2018, **118**(23), 11433–11456.
3 B. Dunn, H. Kamath and J. M. Tarascon, *Science*, 2011, **334**(6058), 928–935.
4 J. Xu, V. Koverga, A. Phan, A. min Li, N. Zhang, M. Baek, C. Jayawardana, B. L. Lucht, A. T. Ngo and C. Wang, *Adv. Mater.*, 2024, **36**, 2306462.
5 H. Zhang, Y. Zhao, X. Li, H. Wang, L. Wang, Y. Song, F. Qiao, J. Wang and J. Xu, *Adv. Sci.*, 2025, **12**(32), e03151.
6 X. Yang, P. Li, C. Guo, W. Yang, N. Zhou, X. Huang and Y. Yang, *J. Power Sources*, 2024, **624**, 235563.
7 J. Wang, W. Huang, A. Pei, Y. Li, F. Shi, X. Yu and Y. Cui, *Nat. Energy*, 2019, **4**(8), 664–670.
8 X. Yang, J. Chen, Q. Zheng, W. Tu, L. Xing, Y. Liao, M. Xu, Q. Huang, G. Cao and W. Li, *J. Mater. Chem. A*, 2018, **6**(33), 16149–16163.
9 J. Hou, M. Yang, D. Wang and J. Zhang, *Adv. Energy Mater.*, 2020, **10**(18), 1904152.
10 W. Zhao, B. Zheng, H. Liu, F. Ren, J. Zhu, G. Zheng, S. Chen, R. Liu, X. Yang and Y. Yang, *Nano Energy*, 2019, **63**, 103815.
11 W. Zhao, G. Zheng, M. Lin, W. Zhao, D. Li, X. Guan, Y. Ji, G. Ortiz and Y. Yang, *J. Power Sources*, 2018, **380**, 149–157.
12 Y. Yin and X. Dong, *Interdiscip. Mater.*, 2023, **2**(4), 569–588.
13 N. Zhang, T. Deng, S. Zhang, C. Wang, L. Chen, C. Wang and X. Fan, *Adv. Mater.*, 2022, **34**(15), 2107899.
14 N. Piao, X. Gao, H. Yang, Z. Guo, G. Hu, H. Cheng and F. Li, *eTransportation*, 2022, **11**, 100145.

15 C. Villevieille, *Nat. Nanotechnol.*, 2025, **20**(1), 2–5.
16 J. Popovic, *Nat. Commun.*, 2021, **12**(1), 6240.
17 Y. Liao, H. Zhang, Y. Peng, Y. Hu, J. Liang, Z. Gong, Y. Wei and Y. Yang, *Adv. Energy Mater.*, 2024, **14**(18), 2304295.
18 S. Hu, H. Zhao, Y. Qian, S. Xiang, G. Zhang, W. Huang, G. Luo, J. Wang, Y. Deng and C. Wang, *J. Energy Storage*, 2023, **57**, 106266.
19 X. Fan and C. Wang, *Chem. Soc. Rev.*, 2021, **50**(18), 10486–10566.
20 K. Xu, *Chem. Rev.*, 2014, **114**(23), 11503–11618.
21 Z. Liu, J. Chai, G. Xu, Q. Wang and G. Cui, *Coord. Chem. Rev.*, 2015, **292**, 56–73.
22 X. Min, C. Han, S. Zhang, J. Ma, N. Hu, J. Li, X. Du, B. Xie, H. Lin, C. Kuo, C. Chen, Z. Hu, L. Qiao, Z. Cui, G. Xu and G. Cui, *Angew. Chem., Int. Ed.*, 2023, **62**(34), e202302664.
23 D. Abraham, M. Furczon, S. Kang, D. Dees and A. Jansen, *J. Power Sources*, 2008, **180**(1), 612–620.
24 J. Eom, I. Jung and J. Lee, *J. Power Sources*, 2011, **196**(22), 9810–9814.
25 T. Hou, G. Yang, N. Rajput, J. Self, S. Park, J. Nanda and K. Persson, *Nano Energy*, 2019, **64**, 103881.
26 M. Kim, H. Moon, S. Kim, Y. Cho, T. Lee, S. Park, H. Kim, Y. Kwon, S. Hong and N. Choi, *Chem. Eng. J.*, 2025, **511**, 162079.
27 B. Nan, L. Chen, N. Rodrigo, O. Borodin, N. Piao, J. Xia, T. Pollard, S. Hou, J. Zhang, X. Ji, J. Xu, X. Zhang, L. Ma, X. He, S. Liu, H. Wan, E. Hu, W. Zhang, K. Xu, X. Yang, B. Lucht and C. Wang, *Angew. Chem., Int. Ed.*, 2022, **61**(35), e202205967.
28 P. Zhou, W. Hou, Y. Xia, Y. Ou, H. Zhou, W. Zhang, Y. Lu, X. Song, F. Liu, Q. Cao, H. Liu, S. Yan and K. Liu, *ACS Nano*, 2023, **17**(17), 17169–17179.
29 H. Li, C. Yan and S. Wang, *EcoEnergy*, 2025, **3**(2), 387–421.
30 Y. Jie, X. Liu, Z. Lei, S. Wang, Y. Chen, F. Huang, R. Cao, G. Zhang and S. Jiao, *Angew. Chem., Int. Ed.*, 2020, **59**(9), 3505–3510.
31 H. Zheng, H. Xiang, F. Jiang, Y. Liu, Y. Sun, X. Liang, Y. Feng and Y. Yu, *Adv. Energy Mater.*, 2020, **10**(30), 2001440.
32 S. Tan, Z. Shadike, J. Li, X. Wang, Y. Yang, R. Lin, A. Cresce, J. Hu, A. Hunt, I. Waluyo, L. Ma, F. Monaco, P. Cloetens, J. Xiao, Y. Liu, X. Yang, K. Xu and E. Hu, *Nat. Energy*, 2022, **7**(6), 484–494.
33 G. Yang, J. Shi, C. Shen, S. Wang, L. Xia, H. Hu, H. Luo, Y. Xia and Z. Liu, *RSC Adv.*, 2017, **7**(42), 26052–26059.
34 Q. Zheng, G. Li, X. Zheng, L. Xing, K. Xu and W. Li, *Energy Environ. Mater.*, 2022, **5**(3), 906–911.
35 M. Liu, Z. Zeng, C. Gu, F. Ma, Y. Wu, Q. Wu, X. Yang, X. Chen, S. Cheng and J. Xie, *ACS Energy Lett.*, 2023, **9**(1), 136–144.
36 N. Y. Yamada, Y. Takazawa, K. Miyazaki and T. Abe, *J. Phys. Chem. C*, 2010, **114**(26), 11680–11685.
37 H. Kim, K. Lim, G. Yoon, J. Park, K. Ku, H. Lim, Y. Sung and K. Kang, *Adv. Energy Mater.*, 2017, **7**(19), 1700418.
38 K. Yoshida, M. Nakamura, Y. Kazue, N. Tachikawa, S. Tsuzuki, S. Seki, K. Dokko and M. Watanabe, *J. Am. Chem. Soc.*, 2011, **133**(33), 13121–13129.
39 Z. Li, N. Yao, L. Yu, Y. Yao, C. Jin, Y. Yang, Y. Xiao, X. Yue, W. Cai, L. Xu, P. Wu, C. Yan and Q. Zhang, *Matter*, 2023, **6**(7), 2274–2292.
40 Y. Wu, Q. Hu, H. Liang, A. Wang, H. Xu, L. Wang and X. He, *Adv. Energy Mater.*, 2023, **13**(22), 2300259.
41 A. Wang, L. Wang, H. Liang, Y. Song, Y. He, Y. Wu, D. Ren, B. Zhang and X. He, *Adv. Funct. Mater.*, 2023, **33**(8), 2211958.
42 Y. Chen, Q. He, Y. Zhao, W. Zhou, P. Xiao, P. Gao, N. Tavajohi, J. Tu, B. Li, X. He, L. Xing, X. Fan and J. Liu, *Nat. Commun.*, 2023, **14**, 8326.
43 Y. Chen, A. Wang, Y. Zhao, W. Wang, R. Dominko, P. Xiao, P. Gao, Y. Duan, B. Li, X. He and J. Liu, *Natl Sci Rev.*, 2026, **13**(3), nwaf543.
44 T. Pham, B. Faheem, K. Kwak and K. Lee, *Batteries Supercaps*, 2025, **8**, e202500163.
45 X. Zheng, Z. Cao, W. Luo, S. Weng, X. Zhang, D. Wang, Z. Zhu, H. Du, X. Wang, L. Qie, H. Zheng and Y. Huang, *Adv. Mater.*, 2023, **35**, 2210115.
46 Y. Zou, Z. Ma, G. Liu, Q. Li, D. Yin, X. Shi, Z. Cao, Z. Tian, H. Kim, Y. Guo, C. Sun, L. Cavallo, L. Wang, H. N. Alshareef, Y.-K. Sun and J. Ming, *Angew. Chem., Int. Ed.*, 2023, **62**, e202216189.
47 Z. Li, Y.-X. Yao, M. Zheng, S. Sun, Y. Yang, Y. Xiao, L. Xu, C.-B. Jin, X.-Y. Yue, T. Song, P. Wu, C. Yan and Q. Zhang, *Angew. Chem., Int. Ed.*, 2025, **64**, e202409409.
48 W. Yang, W. Chen, H. Zou, J. Lai, X. Zeng, Y. Zhang, X. Zeng, K. Ding, S. Zhang, L. Ma, Z. Li and Q. Zheng, *Angew. Chem., Int. Ed.*, 2025, **64**, e202424353.
49 R. Thangavel, V. Ahilan, M. Moorthy, W. Yoon, S. Shanmugam and Y. Lee, *J. Power Sources*, 2021, **484**, 229143.
50 L. Britala, M. Marinaro and G. Kucinskis, *Adv. Energy Mater.*, 2024, **14**(19), 2303468.
51 Y. Chen, W. Zhao, Q. Zhang, G. Yang, J. Zheng, W. Tang, Q. Xu, C. Lai, J. Yang and C. Peng, *Adv. Funct. Mater.*, 2020, **30**(19), 2000396.
52 J. Chen, X. Fan, Q. Li, H. Yang, M. Khoshi, Y. Xu, S. Hwang, L. Chen, X. Ji, C. Yang, H. He, C. Wang, E. Garfunkel, D. Su, O. Borodin and C. Wang, *Nat. Energy*, 2020, **5**, 386–397.
53 Y. Chen, Y. Zhao, A. Wang, D. Zhang, B. Li, X. He, X. Fan and J. Liu, *Energy Environ. Sci.*, 2024, **17**, 6113–6126.
54 Y. Xie, Y. Huang, H. Chen, W. Lin, T. Wu, Y. Wang, S. Liu, M. Sun, H. Huang, P. Dai, Y. Ding, D. Wu, C. Ouyang, Y. Hong, X. Li, C. Liu, S. Liao, L. Huang and S. Sun, *Adv. Funct. Mater.*, 2024, **34**(21), 2310867.
55 L. S. Dodda, I. C. De Vaca and J. Tirado-Rives, LigParGen web server, *Nucleic Acids Res.*, 2017, **45**(W1), W331–W336.
56 S. V. Sambasivarao and O. Acevedo, *J. Chem. Theory Comput.*, 2009, **5**(4), 1038–1050.
57 L. S. Dodda, J. Z. Vilseck and J. Tirado-Rives, *J. Phys. Chem. B*, 2017, **121**(15), 3864–3870.
58 T. Lu, F. Chen and W. Multiwfn, *J. Comput. Chem.*, 2012, **33**(5), 580–592.
59 L. Martínez, R. Andrade and E. G. Birgin, *J. Comput. Chem.*, 2009, **30**(13), 2157–2164.
60 W. Humphrey, A. Dalke and K. Schulten, *J. Mol. Graphics Modell.*, 1996, **14**(1), 33–38.